Available online at www.sciencedirect.com
ScienceDirect
ELSEVIER
Journal of Power Sources 162 (2006) 1192–1202
JOURNAL OF POWER SOURCES
www.elsevier.com/locate/jpowsour

CFD analysis of a solid oxide fuel cell with internal reforming: Coupled interactions of transport, heterogeneous catalysis and electrochemical processes

Vinod M. Janardhanan, Olaf Deutschmann*

Institute for Chemical Technology and Polymer Chemistry, Engesserstr. 20, D-76131 Karlsruhe, University of Karlsruhe (TH), Germany

Received 3 March 2006; received in revised form 24 June 2006; accepted 3 August 2006

Abstract

Direct internal reforming in solid oxide fuel cell (SOFC) results in increased overall efficiency of the system. Present study focus on the chemical and electrochemical process in an internally reforming anode supported SOFC button cell running on humidified CH_4 (3% H_2O). The computational approach employs a detailed multi-step model for heterogeneous chemistry in the anode, modified Butler–Volmer formalism for the electrochemistry and Dusty Gas Model (DGM) for the porous media transport. Two-dimensional elliptic model equations are solved for a button cell configuration. The electrochemical model assumes hydrogen as the only electrochemically active species. The predicted cell performances are compared with experimental reports. The results show that model predictions are in good agreement with experimental observation except the open circuit potentials. Furthermore, the steam content in the anode feed stream is found to have remarkable effect on the resulting overpotential losses and surface coverages of various species at the three-phase boundary.

Keywords: Solid oxide fuel cell; Internal reforming; Methane; Ni-YSZ anode supported; Polarization losses

1. Introduction

The possibility of running hydrocarbons (HCs) with or without pre-reforming make solid oxide fuel cells (SOFCs) unique among all fuel cells. Though the direct use of HCs is desirable from thermodynamic view point, the breakthrough depends on the continuous stable operation of the cell without degradation. This is highly challenging on conventional Ni based anode cermets because of coking propensity. There are many reports on the operation of SOFCs running on H_2 and CH_4 [1–5]. Works on SOFCs running on higher hydrocarbons are also reported [6–8]. Liu and Barnett [5] reported SOFC (LSM-YSZ/YSZ/Ni-YSZ) running on CH_4 and natural gas. The polarization curves reported show identical behavior for both fuels. It could be imputed to the fact that CH_4 is the major constituent of natural gas. Natural gas is an ideal fuel for SOFCs because of the wide spread availability and distribution infrastructure.

The present work mainly focus on the analysis of detailed chemical processes within the anode, electrochemical processes, and losses of SOFCs running on CH_4 rich fuel under internal reforming conditions.

2. Modeling

There are many reports in general on the modeling and simulation of SOFC processes. Most of these models vary in the assumptions made in deriving the model equations and the dimensionality of the problem. Simple one-dimensional models to three-dimensional stack simulations have been reported [9–15]. In a former study [9] we reported the operation of planar SOFC running on pre-reformed CH_4 fuel. The model assumed plug flow in the fuel and air channels and one-dimensional transport in the electrode structures using Dusty Gas Model (DGM). The electrochemistry was implemented using a modified Butler–Volmer setting based on elementary charge transfer chemistry, and the anode chemistry was modeled by a multi-step heterogeneous reaction mechanism.

---

* Corresponding author. Tel.: +49 721 6083138; fax: +49 721 6084805.
E-mail address: deutschmann@ict.uni-karlsruhe.de (O. Deutschmann).

0378-7753/$ – see front matter © 2006 Elsevier B.V. All rights reserved.
doi:10.1016/j.jpowsour.2006.08.017

Nomenclature

A_s	specific catalytic area (m^{-1})
d_p	particle diameter (m)
D^e_{kj}	effective binary diffusion coefficient ($m^2\,s^{-1}$)
$D^e_{k,kn}$	effective Knudsen diffusion coefficient ($m^2\,s^{-1}$)
D^{DGM}_{kl}	DGM diffusion coefficient matrix
E	potential (V), activation energy ($J\,mol^{-1}$)
F	Faraday constant ($C\,mol^{-1}$)
$\vec{F}$	force ($kg\,m^{-2}\,s^{-2}$)
i	current density ($A\,cm^{-2}$)
i_0	exchange current density ($A\,cm^{-2}$)
$\vec{J}$	diffusion flux ($kg\,m^{-2}\,s^{-1}$)
K_r,K_g,K_s	number of reaction, gas-phase species, surface species
l	length (m)
p	pressure (Pa)
r	electrochemical rate ($mol\,m^{-2}\,s^{-1}$)
r_p	pore radius (m)
R	gas constant ($J\,mol^{-1}\,K^{-1}$)
R_{tot}	area specific resistance ($\Omega\,m^2$)
$\dot{s}$	species production rate ($mol\,m^{-2}\,s^{-1}$)
T	temperature (K)
$\vec{v}$	velocity vector ($m\,s^{-1}$)
W	molecular weight ($kg\,mol^{-1}$)
$[X]$	concentration ($mol\,m^{-3}$)
Y_k	mass fraction

Greek symbols

α	permeability (m)
β	symmetry factor
δ_{ij}	Kronecker delta
η	overpotential (V)
μ	viscosity ($kg\,m^{-1}\,s^{-1}$)
ν	stoichiometric coefficient
σ	conductivity ($S\,m^{-1}$)
τ	tortuosity
ϵ	porosity

Subscript

a	anode
c	cathode
e	electrolyte
g	gas
k	species index

Here we resort to model the button cell experiments reported by Liu and Barnett [5]. The experiment describes the operation of an anode supported button cell with 97 vol% CH_4 and 3 vol% H_2O as the fuel stream and air as oxidant. The model presented here solves the velocity $\vec{v}$, pressure p and the species mass fractions Y_k as a function of axial and radial positions, and the electrochemical model parameters. A schematic representation of button cell configuration is shown in Fig. 1, and a two-dimensional plane of which is used as the model geometry. The anode is a 20 mm in diameter and 0.5 mm thick porous membrane. Since the experimental report does not give a detailed description of the flow configuration, the simulation study assumes the inlet fuel pipe to be 7 mm in diameter and ends 5 mm above the anode. The following subsections describe various models used in the present study.

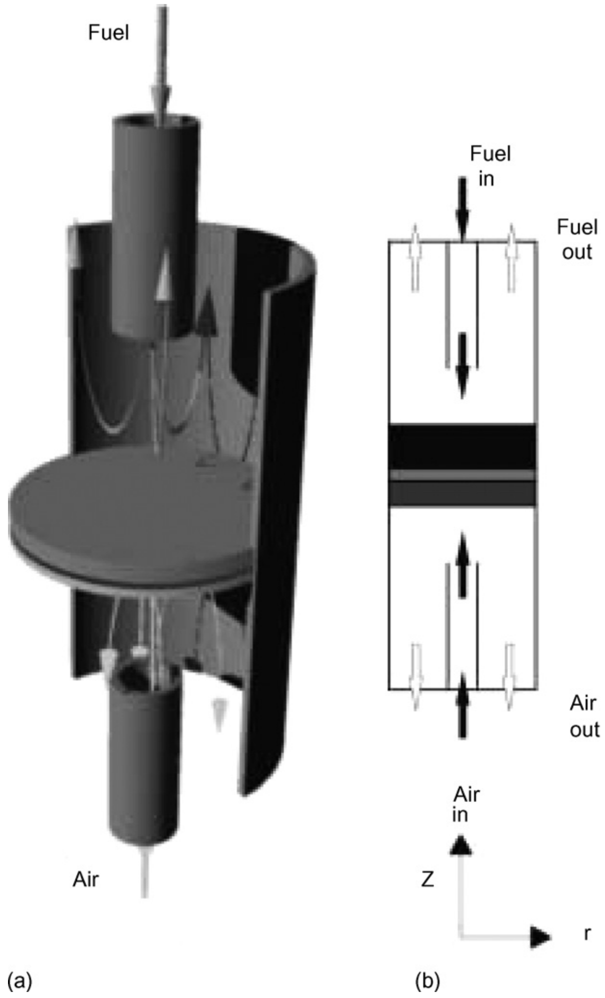

Fig. 1. A three-dimensional schematic representation of button cell configuration (a) and the two-dimensional configuration used for simulation (b).

2.1. Electrochemistry

The electrochemical model assumes that H_2 is the only electrochemically active species, and charge transfer reactions occur only at the interface formed by the electrocatalyst, electrolyte, and gas-phase known as three-phase boundary [16]. In the case of composite electrodes this reaction zone can spread out into the electrode usually of the order of few ~10 μm [1,17]. This is a small fraction of the total thickness of the anode in case of an anode supported cell, and hence we can safely assume that the charge transfer reaction is happening at the well defined three-phase boundary. However, it should be pointed out that increasing the three-phase boundary length is a technology aim [18].

The irreversibility associated with the cell processes lead to various overpotential losses such as activation, ohmic and concentration losses [19]. The operating cell potential is dependent on the overpotential losses and can be written as a function of local current density i.

$$E_{\text{cell}} = E_{\text{rev}} - \eta_{\text{a}}(i) - |\eta_{\text{c}}(i)| - \eta_{\text{ohm}}(i) - \eta_{\text{conc}}(i) \tag{1}$$

where η_{a} and η_{c} are the activation losses at the anode and cathode side, respectively, η_{ohm} the ohmic overpotential, and η_{conc} is the concentration overpotential. Since porous media transport is modeled in detail, the concentration overpotential is not treated explicitly. E_{rev} in Eq. (1) is given by well known Nernst equation.

$$E_{\text{rev}} = E^0 + \frac{RT}{2F} \ln \left(\frac{p_{\text{H}_2,\text{a}} p_{\text{O}_2,\text{c}}^{1/2}}{p_{\text{H}_2\text{O},\text{a}}} \right) \tag{2}$$

In the above equation E^0 is EMF at standard pressure. Eq. (2) can be substituted back in Eq. (1). The ohmic losses in Eq. (1) is defined as

$$\eta_{\text{ohm}} = R_{\text{tot}} i \tag{3}$$

where R_{tot} is the total area specific resistance. However, the resistance offered by the anode and cathode materials are negligible compared to the electrolyte resistance in modern cells. Therefore, in the following analysis only the resistance contributed by the electrolyte R_{e} is considered, which is defined as

$$R_{\text{e}} = \frac{l_{\text{e}}}{\sigma_{\text{e}}}, \tag{4}$$

where l_{e} is the thickness of the electrolyte and σ_{e} is the electrolyte conductivity defined as a function of temperature

$$\sigma_{\text{e}} = 3.34 \times 10^4 \exp \left(-\frac{10300}{T} \right). \tag{5}$$

The above equation is estimated for YSZ electrolyte material and gives an ionic conductivity of 2.26 S/m at 1073 K and 0.086 S/m at 1273 K, which is consistent with the reported values in Ref. [19]. The functional relation between the activation losses and current density is described by a Butler–Volmer formalism. For hydrogen oxidation it takes the form

$$i = i_0 \left[\exp \left(\frac{(1+\beta_{\text{a}}) F \eta_{\text{a}}}{RT} \right) - \exp \left(-\frac{\beta_{\text{c}} F \eta_{\text{a}}}{RT} \right) \right] \tag{6}$$

and for oxygen reduction

$$i = i_0 \left[\exp \left(\frac{\beta_{\text{a}} F \eta_{\text{c}}}{RT} \right) - \exp \left(-\frac{\beta_{\text{c}} F \eta_{\text{c}}}{RT} \right) \right]. \tag{7}$$

where i_0 is the exchange current density and β is the charge transfer coefficient. A detailed derivation of modified Butler–Volmer equations are given elsewhere [9]. In the present study the exchange current density is expressed as a function of temperature and the partial pressures of the reactants and products. The exchange current density for hydrogen oxidation and oxygen reduction is given by Eqs. (8) and (9), respectively [9].

$$i_0 = i_{\text{H}_2}^* \frac{(p_{\text{H}_2}/p_{\text{H}_2}^*)^{1/4} (p_{\text{H}_2\text{O}})^{3/4}}{1 + (p_{\text{H}_2}/p_{\text{H}_2}^*)^{1/2}} \tag{8}$$

and for oxygen reduction

$$i_0 = i_{\text{O}_2}^* \frac{(p_{\text{O}_2}/p_{\text{O}_2}^*)^{1/4}}{1 + (p_{\text{O}_2}/p_{\text{O}_2}^*)^{1/2}} \tag{9}$$

where $i_{\text{H}_2}^*$ and $i_{\text{O}_2}^*$ are adjustable parameter and expressed as a function of temperature by

$$i_{\text{H}_2}^* = k_{\text{H}_2} \exp \left(-\frac{E_{\text{H}_2}}{RT} \right) \tag{10}$$

and

$$i_{\text{O}_2}^* = k_{\text{O}_2} \exp \left(-\frac{E_{\text{O}_2}}{RT} \right). \tag{11}$$

Expressions for $p_{\text{H}_2}^*$ and $p_{\text{O}_2}^*$ can be found in Ref. [9].

2.2. Heterogeneous chemistry

Within a SOFC, anode is the component where the reforming and shift reaction proceeds. There is no significant heterogeneous chemistry proceeding in the cathode and electrolyte. In this work, as reported in Ref. [5] Ni-YSZ is considered to be the anode cermet. Ni is an effective catalyst for steam reforming of hydrocarbons. However, there are issues related to coking under low steam to carbon (s/c) ratio. Kinetics of steam reforming over Ni/$MgAl_2O_4$ based catalysts have been studied by Xu [20]. Studies on internal reforming and related issues in SOFC anodes have been reported by several others [21–24]. Hecht et al. [25] reported a multi-step heterogeneous reaction mechanism for the reforming of CH_4 on Ni catalysts.

In the present work the chemistry is handled by this multi-step heterogeneous reaction mechanism for Ni catalysts. The mechanism consists of 42 reactions among 6 gas-phase species and 12 surface adsorbed species. However, in the study reported by Hecht et al. [25], the mechanism was evaluated only at 800 °C. In this work we use an extended version of the mechanism evaluated for temperatures between 220 and 1700 °C. Though the mechanism is elementary in nature it covers the global aspects of reforming, water–gas shift and Bouduard reaction. Most of the reactions in the mechanism are expressed in Arrhenius rate form and some are dependent on the surface coverage. The rate constants are expressed as

$$k_i = A_i T^{\beta_i} \exp \left(-\frac{E_{ai}}{RT} \right) \prod_{k=1}^{K_{\text{s}}} \theta_k^{\mu_{ki}} \exp \left(-\frac{\epsilon_{ki} \theta_k}{RT} \right) \tag{12}$$

where k_i is the rate constant for the ith reaction, μ_{ki} and ϵ_{ki} the parameters modeling the coverage dependency of rate constant and θ_k is the surface coverage of kth species. The rate of production of each specie is then given by

$$\dot{s}_k = \sum_{i=1}^{K_{\text{r}}} \nu_{ki} k_i \prod_{k=1}^{K_{\text{g}}+K_{\text{s}}} [X]_k^{\nu'_{ki}} \tag{13}$$

where K_{r} is the number of reactions, K_{g} and K_{s} the number of gas-phase species and surface species, respectively, ν_{ki} the difference in stoichiometric coefficients of products and reactants, ν'_{ki} the stoichiometric coefficients of products and $[X]_k$ is the concentration of the kth chemical species. The complete heterogeneous chemistry model is given in Table 1. (The complete mechanism can be downloaded from www.detchem.com/mechanisms.)

At the three-phase boundaries $\dot{s}_k$ also includes the electrochemical production rates for H_2, H_2O and O_2 which are given by

$$r_{H_2} = -\frac{i}{2F}, \qquad r_{H_2O} = \frac{i}{2F}, \qquad r_{O_2} = -\frac{i}{4F} \tag{14}$$

2.3. Fluid transport

The flow field is resolved on a two-dimensional domain with axial and radial coordinate as independent variables and under isothermal conditions. The flow field is computed by solving the equations of continuity

$$\nabla \cdot (\rho \vec{v}) = S_m \tag{15}$$

and momentum

$$\nabla \cdot (\rho \vec{v}\vec{v}) = -\nabla p - \frac{2}{3}\nabla \cdot (\mu \nabla \vec{v}) + \nabla \cdot [\mu(\nabla \vec{v} + \nabla \vec{v}^{T})] + \vec{F}. \tag{16}$$

In Eq. (15) S_m appears only at the three-phase boundary and is the net production of all species given by

$$S_m = \sum_{k=1}^{K_g} \dot{s}_k A_s W_k. \tag{17}$$

In Eq. (16) $\vec{F}$ is zero for the plain media and in the porous media it is defined by Darcy's law as

$$\vec{F} = -\frac{\mu}{\alpha}\vec{v}, \tag{18}$$

where μ is the viscosity and α is the permeability. The species concentrations are solved by the species transport equation defined in the following form:

$$\nabla \cdot (\rho \vec{v} Y_k) = -\nabla \cdot (\vec{J}_k) + \dot{s}_k W_k A_s \tag{19}$$

where Y_k is the mass fraction of kth species in the mixture, $\dot{s}_k$ the molar production rate of the species due to surface reactions defined by Eq. (13), W_k the molecular mass and A_s is the specific area available for surface reactions. The flux $\vec{J}_k$ in Eq. (19) is given by DGM as stated in Ref. [9]

$$\vec{J}_k = -W_k \left[\sum_{l=1}^{K_g} D_{kl}^{DGM} \nabla [X_l] + \left(\sum_{l=1}^{K_g} \frac{D_{kl}^{DGM}[X_l]}{D_{l,kn}^{e}} \right) \frac{\alpha}{\mu} \nabla p \right]. \tag{20}$$

In Eq. (20) first and second term on the right hand side represent the contribution due to diffusive flux and viscous flux, respectively. However, the viscous flux driven by pressure gradient is negligible compared to diffusive flow in the porous anode [2] and is neglected in the following calculations. D_{kl}^{DGM} are defined as the matrix of DGM diffusion coefficients and can be represented as a matrix inverse [9]

$$D_{kl}^{DGM} = H^{-1} \tag{21}$$

where the elements of H matrix are

$$h_{kl} = \left[\frac{1}{D_{k,kn}^{e}} + \sum_{j \neq k} \frac{X_j}{D_{kj}^{e}} \right] \delta_{kl} + (\delta_{kl} - 1)\frac{X_k}{D_{kl}^{e}}. \tag{22}$$

D_{kl}^{e} is the effective binary diffusion coefficient and $D_{l,kn}^{e}$ is the effective Knudsen diffusion coefficient. The effective Knudsen diffusion coefficient is given by

$$D_{l,kn}^{e} = \frac{4}{3}\frac{\epsilon}{\tau} r_p \sqrt{\frac{8RT}{\pi W_k}} \tag{23}$$

where r_p is the pore radius, ϵ the porosity and τ is the tortuosity of the porous medium. The permeability in Eq. (18) is given by Kozeny–Carman relationship

$$\alpha = \frac{\epsilon^3 d_p^2}{72\tau(1-\epsilon)^2} \tag{24}$$

where d_p is the particle diameter.

3. Computational procedure

The flow field is solved using the commercial CFD code FLUENT [28]. However, the source terms and fluxes appearing in Eq. (19) and the electrochemistry model (Eqs. (1), (6), and (7)) are implemented using user defined functions (UDF) [27]. During each iteration the thermodynamic state variables and the species concentrations are accessed from the solver, which are in-turn used to evaluate the UDF returned values. Velocity (0.04 m/s) inlet boundary conditions and pressure outlet boundary conditions are used for the calculations. Eqs. (1), (6) and (7) forms a system of algebraic equations with i, η_a and η_c as unknowns. At three-phase boundary for each computational cell the residual form for the above variables can be written as

$$F(\Phi) = 0 \tag{25}$$

where the vector Φ is ordered as

$$\Phi = [i, \eta_a, \eta_c]. \tag{26}$$

This equation system is solved using damped Newton iterations. The Newton solver normally converges within three to four iterations. However, calculation of residual requires the evaluation of Nernst potential and the exchange current densities which are dependent on the partial pressures of H_2, H_2O and O_2 at the three-phase boundary.

4. Results and discussion

Numerous calculations have been carried out to reproduce the experimental data reported by Liu and Barnett [5]. The parameters used for the calculation are given in Tables 2 and 3. A comparison of experimentally observed and simulated polarization curves is shown in Fig. 2, for the fuel composition of 97 vol% CH_4 and 3 vol% H_2O. In all cases the model reasonably well reproduces the experimental observations. For all operating temperatures we observe a significant drop in cell potential at low current densities, indicating the dominance of activation losses.

Table 1
Reaction mechanism

S.no.	Reaction	A[a] (cm, mol, s)	β	E_a[a] (kJ mol^{-1})
1.	$H_2 + NI(s) + NI(s) \rightarrow H(s) + H(s)$	0.010×10^{-00}[b]	0.0	0.0
2.	$O_2 + NI(s) + NI(s) \rightarrow O(s) + O(s)$	0.010×10^{-00}[b]	0.0	0.0
3.	$CH_4 + NI(s) \rightarrow CH_4(s)$	8.000×10^{-03}[b]	0.0	0.0
4.	$H_2O + NI(s) \rightarrow H_2O(s)$	0.100×10^{-00}[b]	0.0	0.0
5.	$CO_2 + NI(s) \rightarrow CO_2(s)$	1.000×10^{-05}[b]	0.0	0.0
6.	$CO + NI(s) \rightarrow CO(s)$	5.000×10^{-01}[b]	0.0	0.0
7.	$H(s) + H(s) \rightarrow NI(s) + NI(s) + H_2$	$2.545 \times 10^{+19}$	0.0	81.21
8.	$O(s) + O(s) \rightarrow NI(s) + NI(s) + O_2$	$4.283 \times 10^{+23}$	0.0	474.95
9.	$CH_4(s) \rightarrow CH_4 + NI(s)$	$8.705 \times 10^{+15}$	0.0	37.55
10.	$H_2O(s) \rightarrow H_2O + NI(s)$	$3.732 \times 10^{+12}$	0.0	60.79
11.	$CO_2(s) \rightarrow CO_2 + NI(s)$	$6.447 \times 10^{+07}$	0.0	25.98
12.	$CO(s) \rightarrow CO + NI(s)$	$3.563 \times 10^{+11}$	0.0	111.27
	$\theta_{CO(s)}$			−50.0[c]
13.	$H(s) + O(s) \rightarrow OH(s) + NI(s)$	$5.000 \times 10^{+22}$	0.0	97.9
14.	$OH(s) + NI(s) \rightarrow H(s) + O(s)$	$1.781 \times 10^{+21}$	0.0	36.09
15.	$H(s) + OH(s) \rightarrow H_2O(s) + NI(s)$	$3.000 \times 10^{+20}$	0.0	42.7
16.	$H_2O(s) + NI(s) \rightarrow H(s) + OH(s)$	$2.271 \times 10^{+21}$	0.0	91.76
17.	$OH(s) + OH(s) \rightarrow H_2O(s) + O(s)$	$3.000 \times 10^{+21}$	0.0	100.0
18.	$H_2O(s) + O(s) \rightarrow OH(s) + OH(s)$	$6.373 \times 10^{+23}$	0.0	210.86
19.	$C(s) + O(s) \rightarrow CO(s) + NI(s)$	$5.200 \times 10^{+23}$	0.0	148.1
20.	$CO(s) + NI(s) \rightarrow C(s) + O(s)$	$1.354 \times 10^{+22}$	−3.0	116.12
	$\theta_{CO(s)}$			−50.0[c]
21.	$CO(s) + O(s) \rightarrow CO_2(s) + NI(s)$	$2.000 \times 10^{+19}$	0.0	123.6
	$\theta_{CO(s)}$			−50.0[c]
22.	$CO_2(s) + NI(s) \rightarrow CO(s) + O(s)$	$4.653 \times 10^{+23}$	−1.0	89.32
23.	$HCO(s) + NI(s) \rightarrow CO(s) + H(s)$	$3.700 \times 10^{+21}$	0.0	0.0
	$\theta_{CO(s)}$			50.0[c]
24.	$CO(s) + H(s) \rightarrow HCO(s) + NI(s)$	$4.019 \times 10^{+20}$	−1.0	132.23
25.	$HCO(s) + NI(s) \rightarrow CH(s) + O(s)$	$3.700 \times 10^{+24}$	−3.0	95.8
26.	$CH(s) + O(s) \rightarrow HCO(s) + NI(s)$	$4.604 \times 10^{+20}$	0.0	109.97
27.	$CH_4(s) + NI(s) \rightarrow CH_3(s) + H(s)$	$3.700 \times 10^{+21}$	0.0	57.7
28.	$CH_3(s) + H(s) \rightarrow CH_4(s) + NI(s)$	$6.034 \times 10^{+21}$	0.0	61.58
29.	$CH_3(s) + NI(s) \rightarrow CH_2(s) + H(s)$	$3.700 \times 10^{+24}$	0.0	100.0
30.	$CH_2(s) + H(s) \rightarrow CH_3(s) + NI(s)$	$1.293 \times 10^{+22}$	0.0	55.33
31.	$CH_2(s) + NI(s) \rightarrow CH(s) + H(s)$	$3.700 \times 10^{+24}$	0.0	97.1
32.	$CH(s) + H(s) \rightarrow CH_2(s) + NI(s)$	$4.089 \times 10^{+24}$	0.0	79.18
33.	$CH_4(s) + NI(s) \rightarrow C(s) + H(s)$	$3.700 \times 10^{+21}$	0.0	18.8
34.	$C(s) + H(s) \rightarrow CH(s) + NI(s)$	$4.562 \times 10^{+22}$	0.0	161.11
35.	$CH_4(s) + O(s) \rightarrow CH_3(s) + OH(s)$	$1.700 \times 10^{+24}$	0.0	88.3
36.	$CH_3(s) + OH(s) \rightarrow CH_4(s) + O(s)$	$9.876 \times 10^{+22}$	0.0	30.37
37.	$CH_3(s) + O(s) \rightarrow CH_2(s) + OH(s)$	$3.700 \times 10^{+24}$	0.0	130.1
38.	$CH_2(s) + OH(s) \rightarrow CH_3(s) + O(s)$	$4.607 \times 10^{+21}$	0.0	23.62
39.	$CH_2(s) + O(s) \rightarrow CH(s) + OH(s)$	$3.700 \times 10^{+24}$	0.0	126.8
40.	$CH(s) + OH(s) \rightarrow CH_2(s) + O(s)$	$1.457 \times 10^{+23}$	0.0	47.07
41.	$CH(s) + O(s) \rightarrow C(s) + OH(s)$	$3.700 \times 10^{+21}$	0.0	48.1
42.	$C(s) + OH(s) \rightarrow CH(s) + O(s)$	$1.625 \times 10^{+21}$	0.0	128.61

Total surface site density is $\lambda = 2.6 \times 10^{-9}$ mol/cm^2.

[a] Arrhenius parameters for the rate constant written in the form: $k = AT^{\beta} \exp(-E/RT)$.

[b] Sticking coefficient.

[c] Coverage dependent activation energy.

However, the major discrepancy between the model predicted results and the experimentally observed data lies in the open circuit voltages (OCV). The experiment reports maximum OCV of 1.17 at 800 °C. However, the model predicts a much higher OCV (1.55 V) at 800 °C. To validate the model predictions, OCVs are calculated based on equilibrium predictions (with and without surface carbon) assuming H_2 oxidation mechanism. Experimentally observed OCVs are compared with those predicted by the model and equilibrium calculations (Fig. 3). In general though slightly higher, equilibrium composition with surface carbon yields OCVs which are in reasonable agreement with experimental observations. The experimental observation of OCV is lower presumably due to slight gas leakage. However, equilibrium composition without accounting surface carbon results in much higher OCVs. At higher temperatures model predictions are close to those of equilibrium predictions without surface carbon. While at low temperatures model predictions are close to equilibrium calculations with surface carbon. This leads to

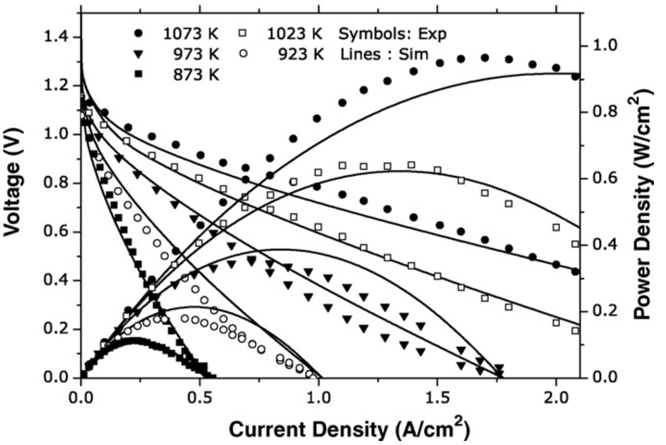

Fig. 2. Voltage and power density against current density. Comparison with experimental data [5].

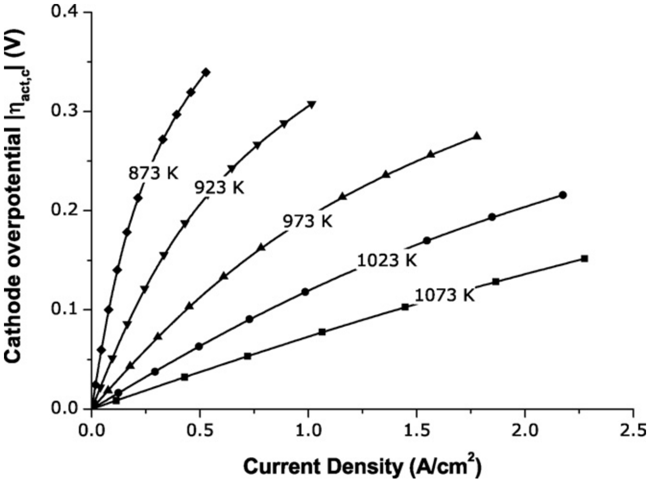

Fig. 4. Cathode overpotentials as a function of current density for different operating temperatures.

the conclusion that, though the surface chemistry model is capable of predicting surface carbon formation, refinement of the model for carbon formation is required for accurate predictions especially at higher temperatures. Nevertheless, it should be noticed that under short-circuit conditions the model is in good agreement with experiments. Liu and Barnett [5] have analyzed a number of possible electrochemical oxidation reactions and concluded that the OCVs for the partial oxidation of C are in good agreement with experimental observations. However, we believe that when enough H_2O is present in the feed, the internal reforming can lead to H_2 production within the anode and under such conditions H_2 oxidation will be the dominant mechanism of electrochemical charge transfer compared to other possible pathways.

Figs. 4 and 5 show the cathodic (η_c) and anodic (η_a) activation losses versus current density. The cathodic activation losses show expected behavior. The losses increase with decreasing temperature and increasing current density. However, the anodic activation loss shows a marked difference from the expected behavior. The anodic losses are distinctly different for high and low temperatures. At high temperatures the losses are high at low current densities. At this point it is worth to analyze the functional dependency of exchange current density i_0. The exchange current density is the current density of charge transfer reaction at equilibrium electric potential difference between the electrode and the electrolyte phases, and is usually a strong function of species composition and temperature. A high exchange current density causes the electrochemical charge transfer reaction to proceed rapidly upon varying the potential difference from its equilibrium value. A careful analysis of Eq. (8) reveals that a zero H_2O partial pressure leads to zero exchange current density. At low current densities, nearly all H_2O produced at the three-phase boundary (TPB) by electrochemical charge transfer reaction is consumed by the reforming chemistry, leading to very low exchange current density for H_2 oxidation. This basically requires high activation overpotential to drive the electrochemical charge transfer reactions. It should be noticed that the activation overpotential η_a is the potential difference above the equilibrium electric potential difference between the electrode and electrolyte phases.

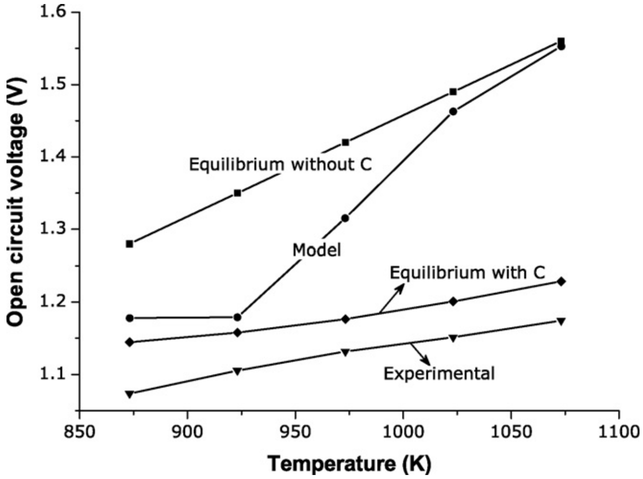

Fig. 3. A comparison of experimentally observed OCVs and those predicted by the model and equilibrium calculations with and without surface carbon formation.

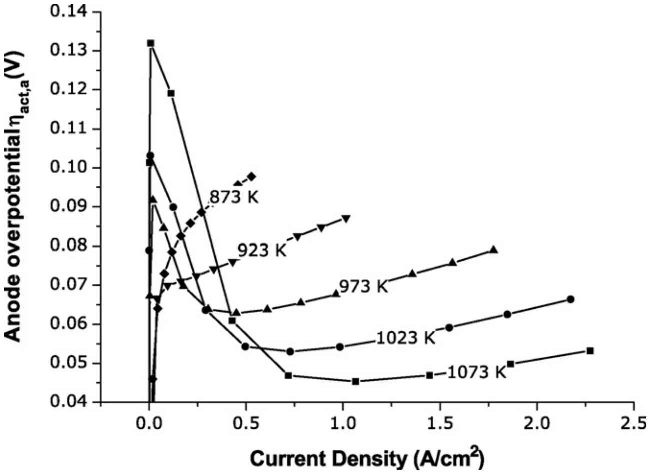

Fig. 5. Anode overpotentials as a function of current density for different operating temperatures.

Table 2
SOFC parameters

Parameters	Values
Anode	
Thickness (l_a, mm)	0.50
Average pore radius (r_p, μm)	0.50
Average particle diameter (d_p, μm)	2.50
Specific area (A_s, cm^{-1})	1025
Porosity (ϵ)	0.35
Tortuosity (τ)	3.80
Charge transfer coefficient (β_a)	0.50
Electrolyte	
Thickness (l_e, μm)	25.0
Cathode	
Thickness (l_c, μm)	30.0
Average pore radius (r_p, μm)	0.50
Average particle diameter (d_p, μm)	2.50
Porosity (ϵ)	0.35
Tortuosity (τ)	3.80
Charge transfer coefficient (β_a)	0.5

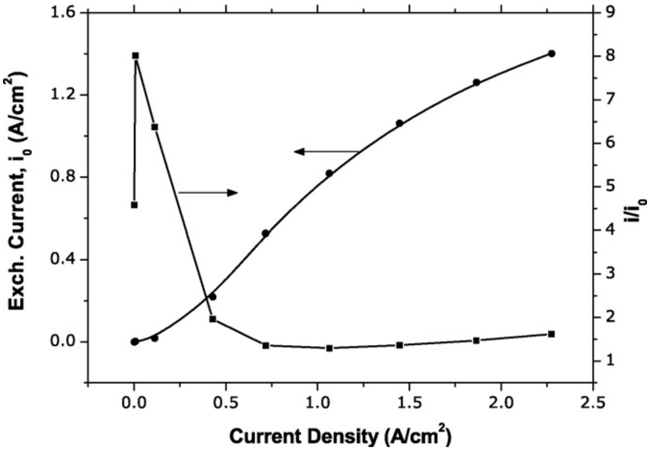

Fig. 6. Exchange current density i_0 and i/i_0 for the anodic branch as a function of current density for the operating temperature of 1073 K.

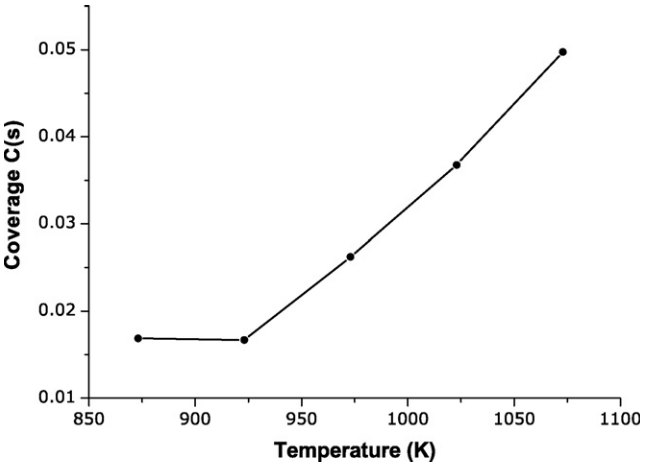

Fig. 7. Surface coverage of carbon at OCVs for different operating temperatures.

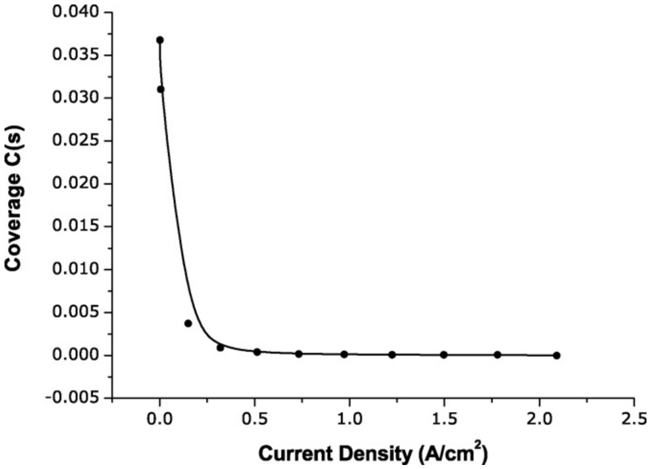

Fig. 8. Carbon formation as a function of current density for the operating temperature of 1023 K.

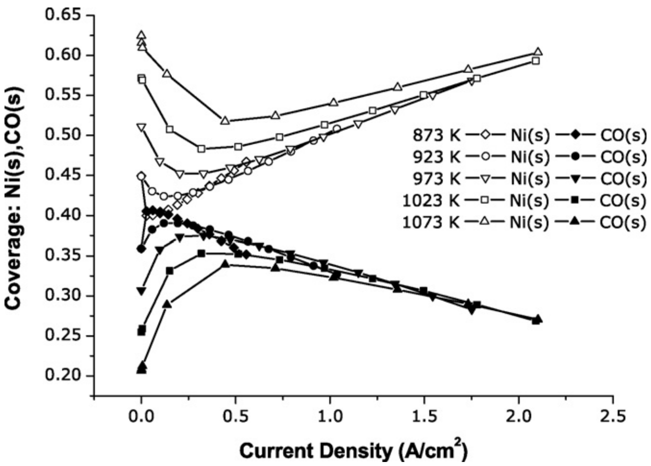

Fig. 9. Fraction of Ni vacancies and surface coverage CO at the three-phase boundary as a function of current density for different operating temperatures.

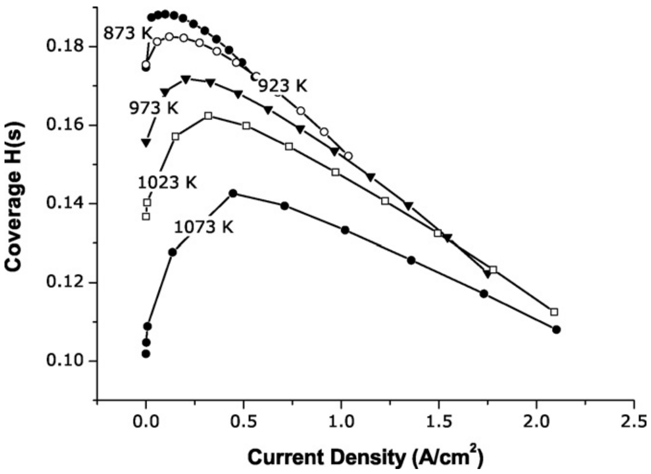

Fig. 10. Surface coverage of hydrogen at the three-phase boundary as a function of current density for different operating temperatures.

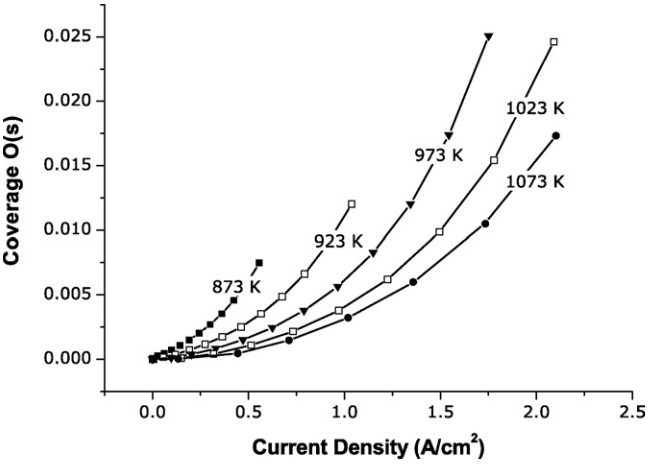

Fig. 11. Surface coverage of oxygen at the three-phase boundary as a function of current density for different operating temperatures.

However, the trend is different at low temperatures, where there is still enough H_2O at the TPB due to the low rate of reforming and hence leading to the expected behavior in loss potential. At high temperatures and high current densities plenty of H_2O available at the TPB and hence the anodic losses shows the expected behavior at high current densities. Though one can argue this behavior is a limiting case of the exchange current density function (Eq. (8)), it is worth remembering that any physically realistic functional formulation of exchange current density should be dependent on the concentration of the reactants and products participating in the charge transfer chemistry [10]. Since H_2 is undoubtedly an electrochemically active species any formulation of exchange current density will be dependent on H_2O partial pressure and will lead to same behavior at low current densities for any fuel with very low H_2O content. A plot of exchange current density i_0 and i/i_0 for the anodic branch is shown in Fig. 6. It is quite clear that the anodic overpotential follows the trend of i/i_0.

Table 3
Parameters for exchange current density

Parameters	Value
H_2 oxidation ($i^*_{H_2}$)	
k_{H_2} (A cm^{-2})	2.07×10^5
E_{H_2} (kJ mol^{-1})	87.8
O_2 reduction ($i^*_{O_2}$)	
k_{O_2} (A cm^{-2})	5.19×10^4
E_{O_2} (kJ mol^{-1})	88.6

Fig. 7 shows the carbon deposition at OCVs for various operating temperatures. Carbon deposition was maximum for the highest operating temperature of 800 °C. Fig. 8 shows carbon formation as a function of current density. It is evident from the figure that the flow of current mitigates coking. It is mainly because of the fact that, as current starts to flow more and more H_2O is formed at the three-phase boundary and hence reducing the possibility of CH_4 cracking on Ni surfaces. This observation of high C deposition at OCV is in good agreement with the experimental report [5]. Surface coverages of other species at the three-phase boundary are shown in Figs. 9–11. Fig. 9 shows the surface coverage of CO and free Ni surfaces. It can be seen that at open circuits the Ni surfaces are relatively open. As current starts flowing the free Ni surfaces are mostly covered by CO and hydrogen (Fig. 10). However, the relative coverage of hydrogen is less compared to CO. The surface coverages of hydrogen can result from the dissociative adsorption of H_2O and CH_4. For all temperature regimes major species on the surface were found to be hydrogen and CO. However, hydrogen coverage was ∼45% of CO coverage for all cases. Fig. 11 shows surface coverages of oxygen. It should be noticed that oxygen on the surface results from the dissociative adsorption of water. For all the species,

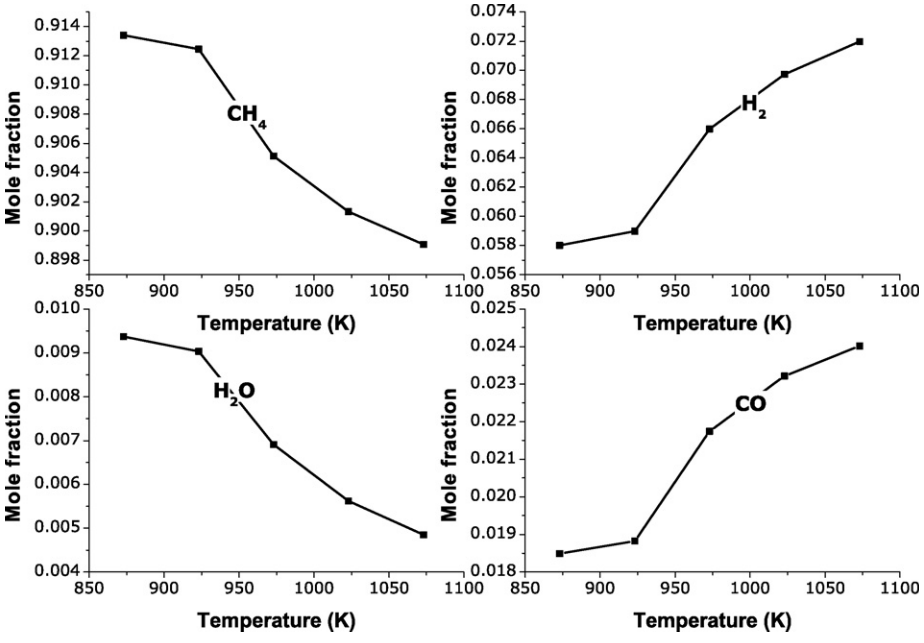

Fig. 12. Composition of anode stream at OCVs as a function of temperature.

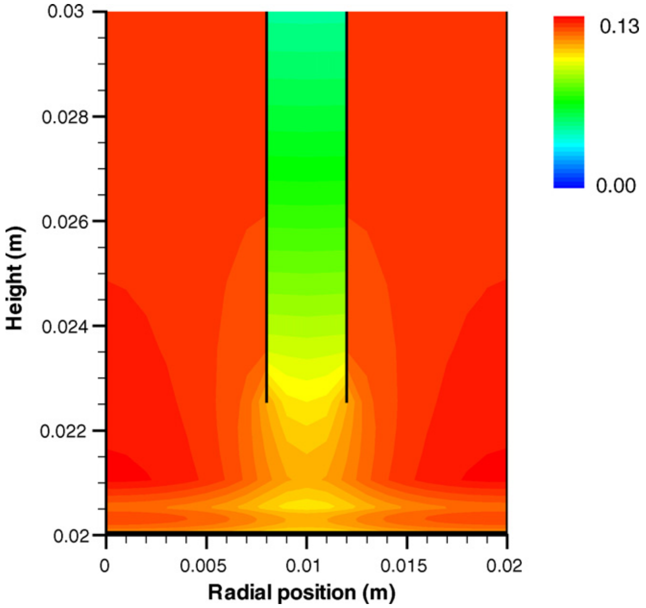

Fig. 13. H_2 mole fractions within the anode compartment.

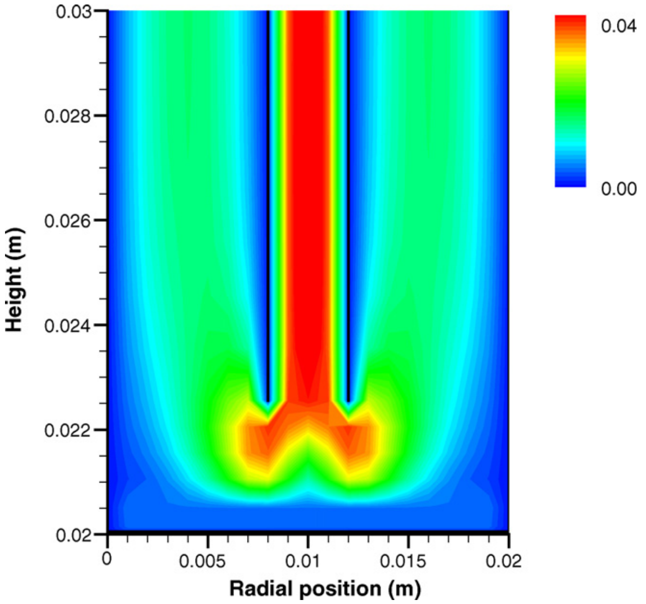

Fig. 15. Velocity (m/s) profiles within the anode compartment.

coverages were found to decrease with increasing temperature. It is obvious that the desorption rates are higher at higher temperature thereby leaving the Ni surfaces open at high temperatures. We believe that carbon formation and its subsequent reaction with H_2O (globally stated as $C + H_2O \Leftrightarrow CO + H_2$) plays a key role at low current densities, where CO and H surface coverages keep increasing. For example, in the case of 750 °C a comparison of surface coverages of H (Fig. 10), CO (Fig. 9), and C reveal that coking is suppressed at current density of $\sim$0.3 A/cm^2 (Fig. 8), and we see a transition in the trend of H and CO coverages at the same current density.

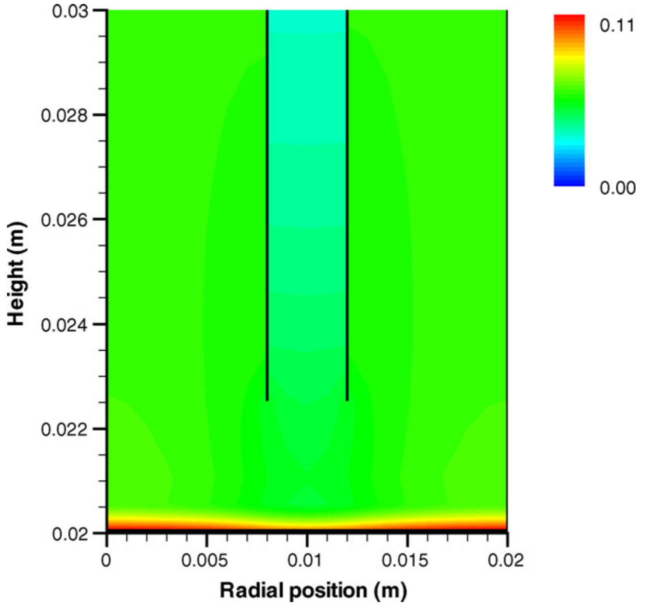

Fig. 14. H_2O mole fractions within the anode compartment.

The composition of anode stream at OCV for various operating temperatures is shown in Fig. 12. Increasing temperature is found to increase all reaction products. CO_2 is omitted from the figure due to its very low concentration at OCVs. Contour plots of H_2 and H_2O mole fractions are shown in Figs. 13 and 14, respectively. It is quite clear that H_2 is produced within the anode and H_2O is produced by the electrochemical charge transfer reaction at the three-phase boundary. It can also be seen

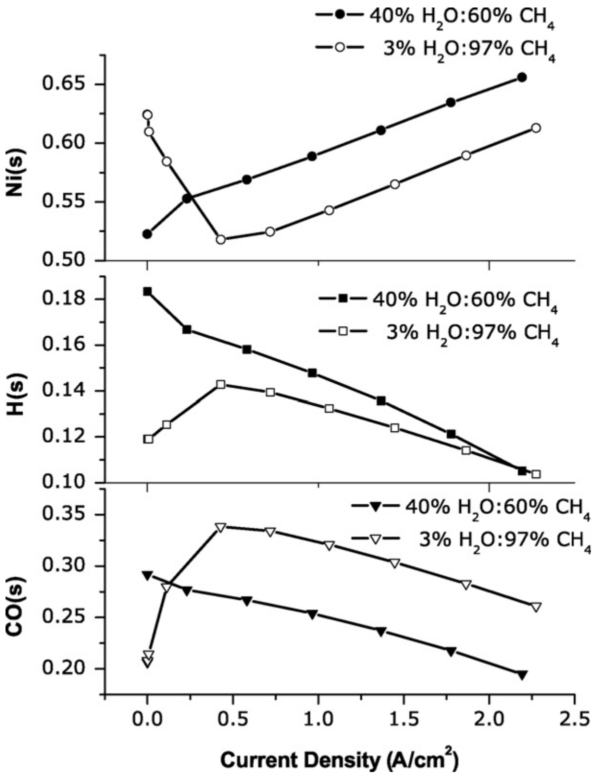

Fig. 16. Comparison of surface coverages of various surface adsorbed species for two different fuel compositions with varying H_2O content.

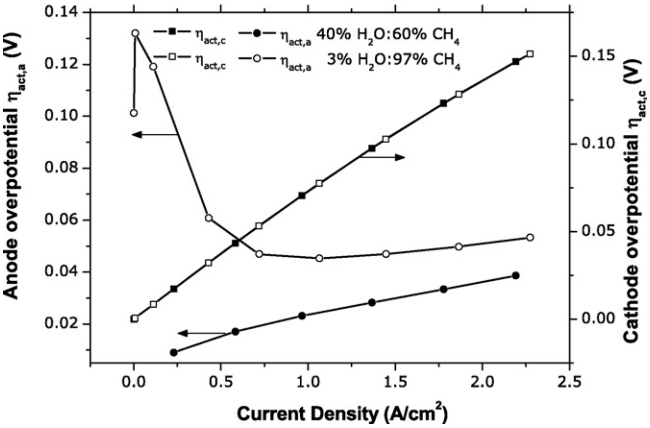

Fig. 17. Comparison of overpotentials for two different inlet fuel compositions with varying H_2O content.

that the very low flow rate causes the back diffusion of H_2 produced within the anode into the fuel inlet channel. For the case of 800 °C velocity profiles within the anode compartment are shown in Fig. 15.

To understand the role of H_2O simulation are carried out with highly humidified CH_4 (40 vol% H_2O). A comparison of surface coverages of H and CO, and empty Ni surface is shown in Fig. 16. Fuel gas with 40% H_2O resulted in higher H coverage and lower CO coverage compared to fuel gas with 3% H_2O. Fig. 17 shows a comparison of activation losses for anode and cathode for the two different feed gas compositions. For the case of fuel gas with 40% H_2O activation overpotentials show a linear behavior with increasing current density and result in a much low activation losses compared to fuel gas with 3% H_2O.

In a recent work Lin et al. [26] reported the exit fuel compositions from a button cell working under the same fuel compositions as in Ref. [5]. They found all the products to be increasing with increasing current density, though the equilibrium calculation predicts different trend. However, data is reported only for lower current densities (up to 0.8 A/cm^2). Our findings also predict an increasing product composition at low current densities (up to 0.5 A/cm^2) and then a decreasing H_2 and CO concentrations for further increase in current densities (Fig. 18). However, our calculations predict more H_2O than CO_2, while the experiment predicts higher CO_2 than H_2O. Our prediction of higher H_2O than CO_2 is consistent with the equilibrium predictions.

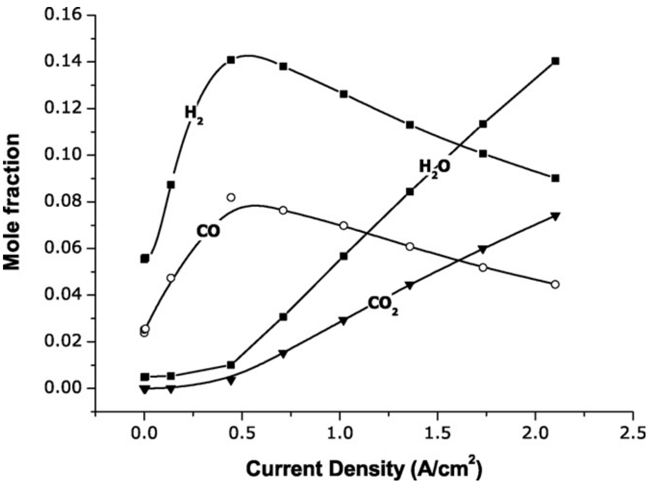

Fig. 18. Exit gas composition as a function of current density at 800 ° for the case of 97% CH_4 and 3% H_2O.

5. Conclusions

In the present work a detailed CFD study of the chemical and electrochemical processes in an internally reforming anode supported SOFC button cell was carried out. We have implemented detailed models for chemistry, electrochemistry and porous media transport into the commercial CFD code FLUENT. Simulation results were compared with experimentally reported data. The comparisons lead to the conclusion that precise calculation of surface carbon formation is critical for the accurate prediction of OCVs for hydrocarbon fuels with very low H_2O content. Anodic overpotentials showed remarkable difference from expected behavior. Though there are no experimental findings to validate our findings on the anodic loss potentials, any functional form of exchange current density cited so far in the literature (e.g. [10,32]) would lead to the same trend as reported here. Within the framework of simulation, the well understood aspects are the flow field models and the reforming chemistry. The heterogeneous chemistry model used in this work is well validated for Ni-YSZ cermets by Hecht et al. [25]. There is no question on the validity of Navier Stokes equations for fluid transport. DGM have been used by many researchers for porous media transport [9,29,30]. However, electrochemistry remains as one of the least understood aspect of fuel cell modeling. As done in this work most the modeling effort uses Butler–Volmer formalism, except some state space modeling works [31,33]. Any deviation from physically realistic behavior can raise questions on the validity of existing electrochemical models, which can be well applied for any fuel composition. The model presented here is well applicable for any fuel cell configuration and can be applied to understand the underlying chemical and physical processes and hence to choose the best operating conditions for SOFCs.

Acknowledgments

We gratefully acknowledge many fruitful discussions with Professor R.J. Kee and Dr. Huyang Zhu (Colorado School of Mines). We are also thankful to Dr. Luba Maier (University of Karlsruhe) for providing us with the improved heterogeneous chemistry mechanism prior to its publication.

References

[1] J.W. Kim, A.V. Vikar, K.Z. Fung, K. Mehta, S.C. Singhal, J. Electrochem. Soc. 146 (1999) 69–78.
[2] Y. Jiang, A.V. Virkar, J. Electrochem. Soc. 150 (2003) A942–A951.
[3] E.P. Murray, T. Tsai, S.A. Barnett, Nature 400 (1999) 649–651.
[4] S. Park, J.M. Vohs, R.J. Gorte, Nature 404 (2000) 265–267.
[5] J. Liu, S.A. Barnett, Solid State Ionics 158 (2003) 11–16.
[6] N.M. Sammes, R.J. Boersma, G.A. Tompsett, Solid State Ionics 135 (2000) 487–491.
[7] Z. Zhan, S.A. Barnett, Solid State Ionics 176 (2005) 871–879.
[8] Z. Zhan, S.A. Barnett, Science 308 (2005) 844–847.

[9] H. Zhu, R.J. Kee, V.M. Janardhanan, O. Deutschmann, D. Goodwin, J. Electrochem. Soc. 152 (2005) A2427–A2440.

[10] P. Costmagna, A. Selimovic, M.D. Borghi, G. Agnew, Chem. Eng. J. 102 (2004) 61–69.

[11] K. Keegan, M. Khaleel, L. Chick, K. Recknagle, S. Simmer, J. Deibler, SAE Technical Paper Series, 2002–01-0413.

[12] B.A. Haberman, J.B. Young, Int. J. Heat Mass Transfer 47 (2004) 3617–3629.

[13] P. Costamagna, K. Honegger, J. Electrochem. Soc. 145 (1998) 3995–4007.

[14] P.W. Li, L. Schaefer, M.K. Chyu, J. Heat transfer 126 (2004) 219–229.

[15] D.J. Hall, IEEE Trans. Energy Conversion 14 (1999) 749–753.

[16] C.W. Tanner, K.Z. Fung, A.V. Virkar, J. Electrochem. Soc. 144 (1997) 21–30.

[17] R.E. Williford, L.A. Chick, G.D. Maupin, S.P. Simmer, J.W. Stevenson, J. Electrochem. Soc. 150 (2003) A1067–A1072.

[18] M. Brown, S. Primdhal, M. Mogensen, J. Electrochem. Soc. 147 (2000) 475–485.

[19] J. Larminie, A. Dicks, Fuel Cell Systems, second ed., John Wiley and Son, 2003.

[20] J. Xu, G.F. Froment, AIChE 35 (1989) 8–35.

[21] C.M. Finnerty, N.J. Coe, R.J. Cunningham, R.M. Ormerod, Catal. Today 46 (1998) 137–145.

[22] S.H. Clarke, A.L. Dicks, K. Pinton, T.A. Smith, A. Swann, Catal. Today 35 (1997) 411–423.

[23] K. Ahmed, K. Foger, Catal. Today 63 (2000) 479–487.

[24] A.L. Dicks, K.D. Pointon, A. Siddle, J. Power Sources 86 (2000) 523–530.

[25] E.S. Hecht, G.K. Gupta, H. Zhu, A.M. Dean, R.J. Kee, L. Maier, O. Deutschmann, Appl. Catal. A 295 (2005) 40–51.

[26] Y. Lin, Z. Zhan, J. Liu, S.A. Barnett, Solid State Ionics 176 (2005) 1827–1835.

[27] O. Deutschmann, S. Tischer, S. Kleditch, V.M. Janardhanan, C Correa, D. Chatterjee, J. Warnatz, DETCHEM User Manual Version 2.0, 2004, www.detchem.com.

[28] FLUENT User Manual Version 6.1.

[29] R.B. Evans, G.M. Watson, E.A. Mason, J. Chem. Phys. 36 (1962) 1894–1902.

[30] R. Krishna, Chem. Eng. J. 35 (1987) 75–81.

[31] W.G. Bessler, S. Gewies, J. Warnatz, Electrochem. Soc. Proc. 7 (2007) 709–718.

[32] W.G. Bessler, D.G. Goodwin, J. Warnatz, “The Influence of Equilibrium Potential on Electrochemical Kinetics of SOFC Anodes” P0708, Seventh European Solid Oxide Fuel Cell Forum, July 3–7, 2006, Lucerne/Switzerland.

[33] D. Goodwin, Electrochem. Soc. Proc. 7 (2007) 699–707.